Received: 14 July 2021 | Revised: 9 September 2021 | Accepted: 4 October 2021

DOI: 10.1002/mrm.29056

RESEARCH ARTICLE

Magnetic Resonance in Medicine

# Pulse encoding for ZTE imaging: RF excitation without dead-time penalty

**Romain Froidevaux** | **Markus Weiger** | **Klaas P. Pruessmann**

Institute for Biomedical Engineering, ETH Zurich and University of Zurich, Zurich, Switzerland

**Correspondence**
Markus Weiger, Institute for Biomedical Engineering, ETH Zurich and University of Zurich, Gloriastrasse 35, 8092 Zurich, Switzerland.
Email: weiger@biomed.ee.ethz.ch

**Purpose:** To overcome limitations in the duration of RF excitation in zero-TE (ZTE) MRI by exploiting intrinsic encoding properties of RF pulses to retrieve data missed during the dead time caused by the pulse.

**Methods:** An enhanced ZTE signal model was developed using multiple RF pulses, which enables accessing information hidden in the pulse-induced dead time via encoding intrinsically applied by the RF pulses. Such ZTE with pulse encoding was implemented by acquisition of two ZTE data sets using excitation with similar frequency-swept pulses differing only by a small off-resonance in their center frequency. In this way, the minimum scan time is doubled but each acquisition contributes equally to the SNR, as with ordinary averaging. The method was demonstrated on long-$T_2$ and short-$T_2$ phantoms as well as in in vivo experiments.

**Results:** ZTE with pulse encoding provided good image quality at unprecedented dead-time gaps, demonstrated here up to 6 Nyquist dwells. In head imaging, the ability to use longer excitation pulses led to approximately 2-fold improvements in SNR efficiency as compared with conventional ZTE and allowed the creation of $T_1$ contrast.

**Conclusion:** Exploiting intrinsic encoding properties of RF pulses in a new signal model enables algebraic reconstruction of ZTE data sets with large dead-time gaps. This permits larger flip angles, which can be used to achieve enhanced $T_1$ contrast and significant improvements in SNR efficiency in case the Ernst angle can be better approached, thus broadening the range of application of ZTE MRI.

**KEYWORDS**

algebraic reconstruction, dead-time gap, pulse encoding, sweep pulse, ZTE

## 1 | INTRODUCTION

There exists a variety of tissues with short transverse relaxation times $T_2$ or $T_2^*$ in the sub-millisecond range, such as bone,[1,2] teeth,[3,4] lung,[5–7] or myelin.[8–10] Imaging of such components requires rapid spatial encoding and early signal acquisition,[11] which are two traits of zero-TE (ZTE) MRI.[12,13] In the ZTE pulse sequence, a radial readout gradient is activated before RF excitation to immediately encode transverse magnetization, whereas MR signal is

probed as soon as possible after switching the RF chain from transmit to receive state.

This sequence design poses two major challenges: (1) RF excitation is spatially selective, which must be counteracted by using high-bandwidth pulses (i.e., either short hard or longer frequency-swept pulses); and (2) the early-encoded signal cannot be detected during excitation and until the RF chain is in receive state. Data missed during this dead time leads to a central gap in k-space and must therefore be complemented to avoid related image artifacts. This can be accomplished either during image reconstruction as in algebraic ZTE,[12] or with additional acquisitions at lower gradient strength as in pointwise encoding time reduction with radial acquisition (PETRA),[14] water-suppressed and fat-suppressed proton projection MRI,[15] or ZTE with hybrid filling.[16]

The latter three techniques have shown promising results, but the extra scan time required lowers their SNR efficiency, and artifacts related to discontinuous $T_2^*$ weighting in k-space may occur.[17] Furthermore, the additional acquisitions necessitate adjustments of gradient amplitude that increase acoustic noise and eddy currents, thus impairing some of the intrinsic beneficial features of the ZTE sequence.

On the other hand, algebraic ZTE is limited to dead-time gaps up to approximately three Nyquist dwells $dt = 1/BW$ (with imaging bandwidth $BW$), beyond which large amplification of noise and out-of-band signal occurs.[18] Hence, at large $BW$, as required for high-resolution imaging of short-$T_2$ tissues, only short RF pulses can be used, thus imposing limits on achievable flip angles and thereby potentially on SNR and contrast.

In this work, a new strategy is introduced for algebraic ZTE MRI that allows elimination of the contribution of the RF pulse from the dead time. This is achieved by giving the pulse an active role in spatial encoding by exploiting its property of correlating neighboring data, similar to coil sensitivities in parallel imaging. The concept goes beyond current mere pulse correction approaches[14,19,20] by using excitation with slightly differing RF pulses and an accordingly expanded signal model, which enables recovering signal missed during the pulse-related dead time. Bandwidth limitations are then exclusively given by the time to switch from transmit to receive operation. In this way, the novel pulse-encoded ZTE (PE-ZTE) technique permits the use of longer excitation pulses.

The PE-ZTE method was implemented by the acquisition of two full ZTE data sets with pulses differing by a small off-resonance. In this way, the minimum scan time is doubled, but the SNR efficiency is preserved or even improved due to a potentially increased steady-state magnetization by using larger flip angles. The latter also permits the creation of $T_1$ contrast, thus widening the range of applications of algebraic ZTE MRI while maintaining its beneficial properties. The feasibility of PE-ZTE is demonstrated on long-$T_2$ and short-$T_2$ phantoms as well as in head imaging, confirming the expected improvements in SNR and $T_1$ contrast as compared with conventional algebraic ZTE.

## 2 | METHODS

Figure 1 shows the basic 3D radial ZTE sequence, in which after ramping up the gradient, RF excitation is performed with either short hard pulses of maximum duration of approximately $1/BW$ or longer sweep pulses. From data sets obtained in this manner, images can be reconstructed by algebraic treatment,[12,21–23] which is also the basis for PE-ZTE and therefore summarized subsequently.

### 2.1 | General reconstruction strategy

To reduce computational demands, ZTE reconstruction is split into two steps (Figure 2): (1) recovery of missing samples by linear combination of acquired data along each radial direction, and (2) 3D image reconstruction.

For the first step, the signal equation is written in matrix-vector form as $\boldsymbol{s} = \boldsymbol{E}\boldsymbol{\rho}$, with the acquired radially oversampled signal $\boldsymbol{s}$, the encoding matrix $\boldsymbol{E}$, and the projection $\boldsymbol{\rho}$ of the object along the encoding gradient direction. Then an intermediate one-dimensional (1D) image $\hat{\boldsymbol{\rho}} = \boldsymbol{F}\boldsymbol{s}$ is reconstructed using the pseudoinverse of the encoding matrix $\boldsymbol{F} = \boldsymbol{E}^{\dagger}$. The corresponding reconstructed data $\hat{\boldsymbol{s}}$ includes the initially missed signal and is computed by Fourier-transforming the intermediate image: $\hat{\boldsymbol{s}} = i\boldsymbol{F}\boldsymbol{T}\,\hat{\boldsymbol{\rho}} = i\boldsymbol{F}\boldsymbol{T}\boldsymbol{F}\boldsymbol{s}$. The entire 1D procedure can therefore be assembled in a single linear operation by using a matrix of coefficients as follows[18]:

$$\boldsymbol{C} = i\boldsymbol{F}\boldsymbol{T}\boldsymbol{F} \tag{1}$$

such that $\hat{\boldsymbol{s}} = \boldsymbol{C}\boldsymbol{s}$.

The second step consists of a standard 3D reconstruction for non-Cartesian data that includes gridding of all reconstructed 1D spokes $\hat{\boldsymbol{s}}$ onto a Cartesian grid, followed by 3D Fourier transform to image space, optionally combined with an iterative conjugate gradient algorithm for improved density correction.[24]

### 2.2 | Encoding matrices

#### 2.2.1 | ZTE with hard pulse

Using short hard pulses permits the assumption of instantaneous excitation in creating a single coherence that

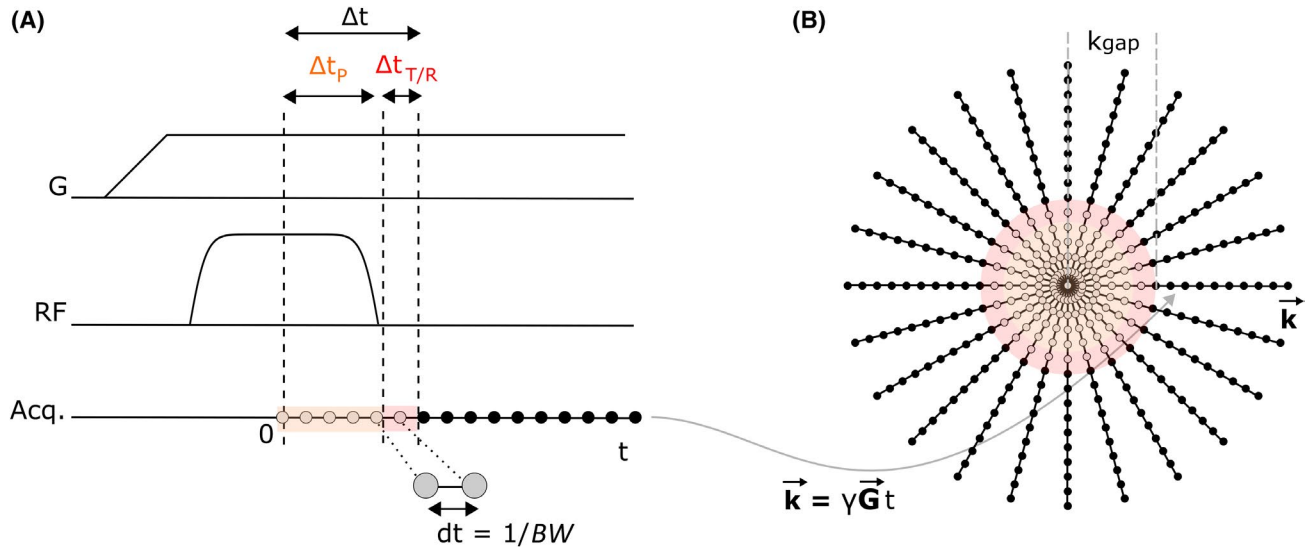


**FIGURE 1** Zero-TE (ZTE) pulse sequence. (A) After ramping up the gradient $G$, RF excitation is performed and data are acquired after the dead time $\Delta t$ (here, 6 Nyquist dwells $dt$), which includes half the pulse duration $\Delta t_p$ and the transmit-receive switching time $\Delta t_{T/R}$. (B) The 3D k-space (one central plane shown) is probed radially in a center-out fashion by varying the gradient direction. However, due to the dead time, a spherical region of radius $k_{gap}$ surrounding the origin cannot be accessed and needs to be complemented in a suitable way. Abbreviation: $BW$, bandwidth

evolves as one line in k-t space (Figure 3A). In this case, the encoding matrix is described by

$$\boldsymbol{E}^{\pm}_{m,j} = \exp\left(\pm i\, k_m r_j\right) \tag{2}$$

with ± indicating the polarity of the readout gradient $G$, k-space variable $k = \gamma G t$, acquisition time $t$, and position variable $r$. Indices $m$ and $j$ identify the discrete samples in k-space and image space, respectively.

The first k-space point acquired after the dead-time gap is

$$k_{gap} = \gamma\, G\, \left(\Delta t_p + \Delta t_{T/R}\right) = \Delta k_p + \Delta k_{T/R} \tag{3}$$

where the labels $p$ and $T/R$ indicate the individual contributions from pulse and transmit-receive switching, respectively.

### 2.2.2 | ZTE with sweep pulse

At limited RF power, larger flip angles than with a hard pulse may be achieved by using modulated RF excitation using a frequency sweep over $BW$.[20,25] However, a frequency-swept pulse induces an approximately quadratic phase in image space that needs appropriate correction. To this end, it may be represented as a train of discrete hard pulses with complex amplitude, each creating its own coherence (Figure 3B).[21] Thus, several coherences exist at the same time and all contribute to the total MR signal. The latter can then be viewed as the result of the convolution of a single coherence with the pulse shape $p(t)$ (Supporting Information A), and acquired samples are correlated over a period equal to the total pulse duration $2\Delta t_p$. For the sweep case, the encoding matrix expands to

$$E^{\pm}_{m,j} = \sum_l p_l \exp\left(\pm i\,\gamma\, \left(t_m - \tau_l\right) G r_j\right) \tag{4}$$

where $p_l (l = 1, 2\cdots, L)$ is the discretized pulse shape, $L$ is the total number of pulse samples and $t_m$ is the time after the pulse center when the $m$th data point is acquired. The first acquired data sample contains k-space information down to

$$k_{gap} = \gamma\, G\, \left(\Delta t_p + \Delta t_{T/R} - \Delta t_p\right) = \Delta k_{T/R}, \tag{5}$$

which is independent on pulse duration.

This signal model for extended pulses requires the definition of boundary conditions at the borders of the k-space support to handle excessively modulated coherences (Supporting Information A).[21] Throughout the present work, the established option of neglecting the latter was chosen.

Despite the refined signal model including pulse information and reaching in k-space down to $\Delta k_{T/R}$, in practice, sweep ZTE reconstruction hits similar limits as ZTE with hard pulses. In fact, as long as a single pulse is considered in the signal model, it can be shown (Supporting Information A) that inverting the forward model of Equation 4 is equivalent to first reconstructing an image assuming instantaneous excitation and then correcting for the pulse in image space by division with the pulse spectrum. Hence, the pulse

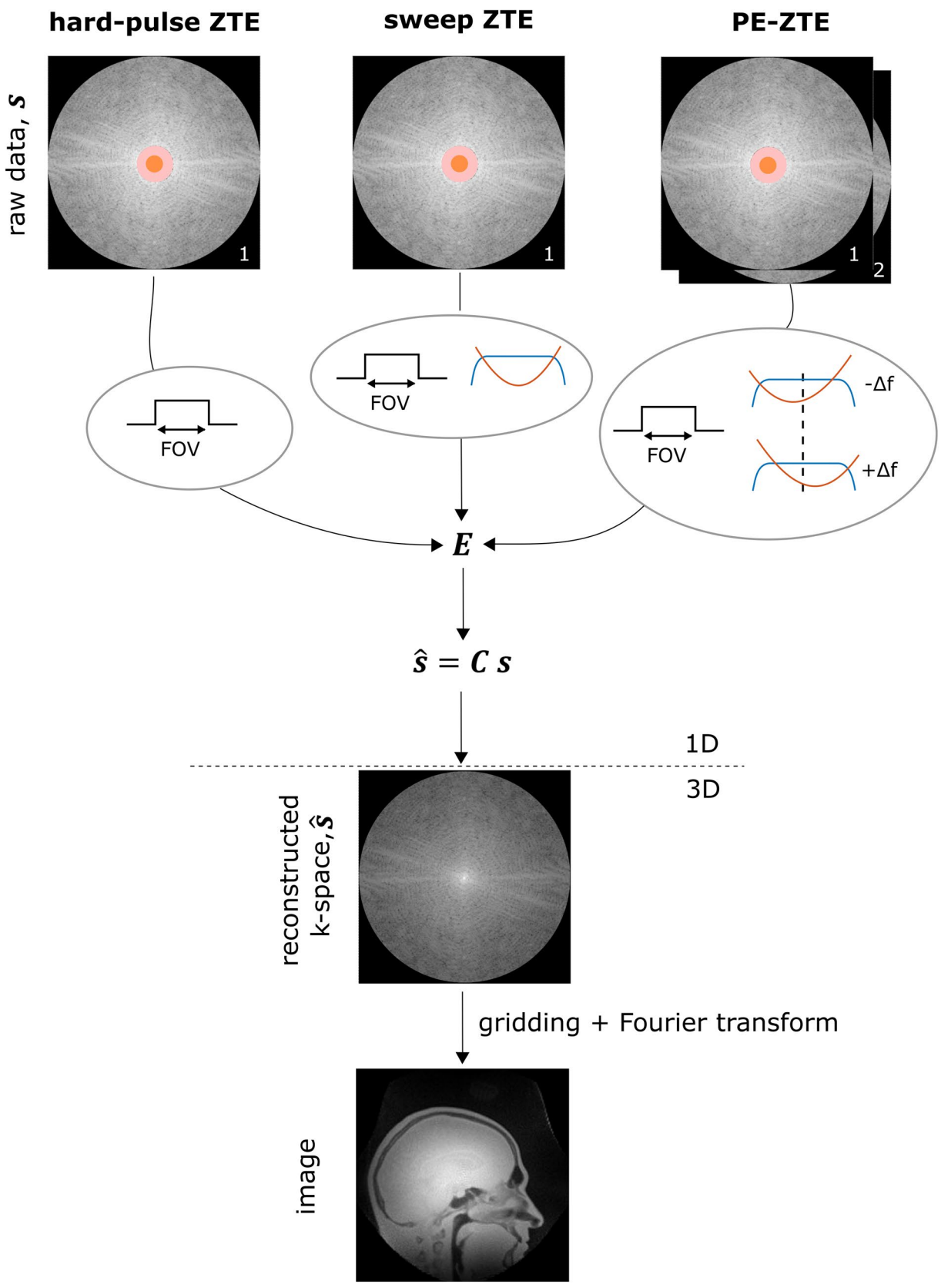


information is only considered after the image has been reconstructed and is therefore ineffective in retrieving data missed during the pulse.

Note that application of the signal model introduced for sweep excitation in case of pulses without frequency modulation corresponds to the hard-pulse approach but

**FIGURE 2** Zero-TE image reconstruction. For hard-pulse ZTE, the raw data $\boldsymbol{s}$ are acquired once and the encoding matrix $\boldsymbol{E}$ is computed assuming finite support (i.e., that all signal stems from inside the FOV). No pulse information is introduced into the signal model. The missing data are extrapolated per direction in one dimension (1D) by multiplication with the matrix $\boldsymbol{C} = i\boldsymbol{F}\boldsymbol{T}\,\boldsymbol{F}$ (with the inverse Fourier transform operator $i\boldsymbol{F}\boldsymbol{T}$ and the pseudo inverse of the encoding matrix $\boldsymbol{F}$). Then, gridding and Fourier transform are used to reconstruct the final 3D image. For sweep ZTE, the reconstruction procedure is identical to ZTE, except that the pulse shape is introduced into the signal model, primarily to correct for the pulse phase. For pulse-encoded ZTE (PE-ZTE), the new approach differs from sweep ZTE in that (1) raw data are acquired twice with identical pulses apart from off-resonances $\pm\Delta f$, and (2) the knowledge about the two pulses is included in $\boldsymbol{E}$

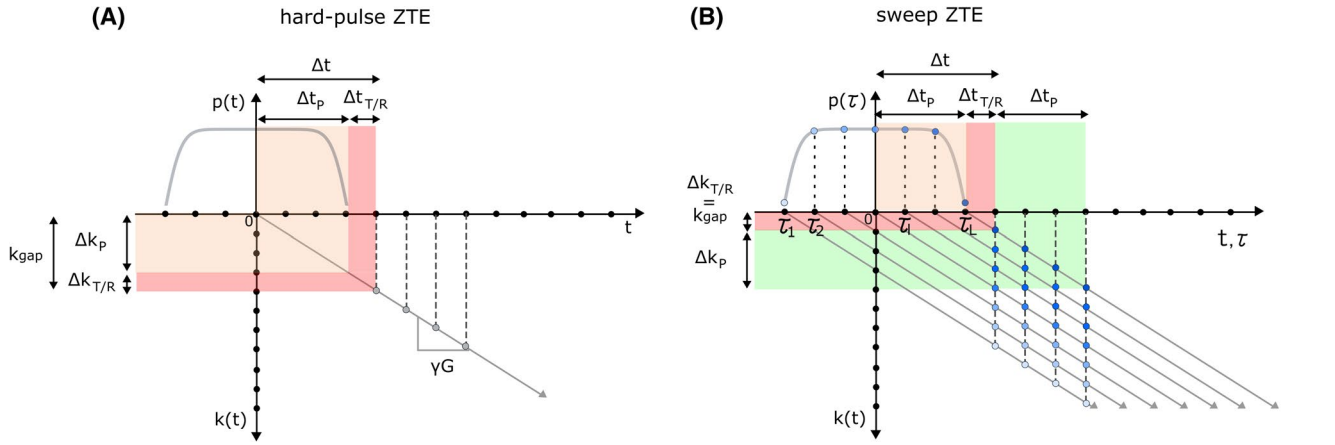


**FIGURE 3** Radiofrequency pulses in the ZTE signal model. (A) In hard-pulse ZTE, a single coherence is assumed to be created by an infinitely short pulse at $t = 0$. As the gradient strength is kept constant during encoding, the created coherence evolves along a linear trajectory in k-t space ($k = \gamma G t$). Data acquisition is only possible after the dead time $\Delta t$ that includes half of the actual pulse duration $\Delta t_p$ and the transmit-receive switching time $\Delta t_{T/R}$. Hence, the k-space can only be probed at k-values larger than $k_{gap} = \Delta k_p + \Delta k_{T/R} = \gamma G\,(\Delta t_p + \Delta t_{T/R})$. (B) In sweep ZTE, the pulse can be considered a series of $L$ infinitely short hard pulses sent at $t = \tau_l$ (with $l = 1, 2, \ldots, L$) with complex amplitudes $p(\tau)$, each creating its own coherence. In this way, the data acquired at a given time are the sum of coherences associated with different k-space locations, which span a range of $2\Delta k_p$. Hence, the same k-space point appears with different weightings in several data points over a duration $2\Delta t_p$, where the weightings are the complex amplitudes of the subpulses. In addition, the inner k-space information located in a region of size $\Delta k_p$ is acquired during a period $\Delta t_p$ following the pulse (green region). Note that subpulses are shown on the grid of the sampled data for convenience but may also be described on another grid, provided that the Nyquist criterion is fulfilled

with correction for intensity variations associated with finite pulse duration similar to Grodzki et al.[26]

## 2.3 | ZTE with pulse encoding

To enable actually using pulse information for gap filling, multiple pulses need to be present in the signal model. In this case, separate pulse correction in image space cannot work anymore and the pulses join in for gap filling (Supporting Information A). To implement this concept, we propose acquiring all data twice, each time with a different pulse. In this way, each acquisition contributes equally to the SNR, as with ordinary averaging. The encoding matrix becomes

$$E^{\pm}_{(q,m),j} = \sum_l p_{q,l} \exp\left(\pm i\gamma\,\left(t_m - \tau_l\right) G r_j\right), \qquad (6)$$

which corresponds to stacking of two matrices as defined in Equation 4, each holding a different pulse with index $q$.

By adding a second pulse in the signal model, well-conditioned reconstruction becomes feasible, with only little dependence on pulse length. However, the choice of a suitable pulse pair is critical to achieve optimal conditioning.

Three main factors must be considered for pulse selection. First, as always for ZTE techniques, excitation should be sufficiently uniform over the whole 3D FOV,[26] a feature that can be provided by sweep pulses. Second, the flip angles for the two acquisitions should be very similar to prevent differences in signal levels. Hence, either the pulse length should be kept constant or the pulse power needs to be adapted. Third, the pulses should be sufficiently diverse to add independent information to the signal model. With the mentioned restrictions on pulse length and amplitude, the easiest way to make the two pulses different is

to modify their phase, which can be done by shifting their center frequency.

The consequences of such a shift are illustrated in Figure 4, where off-resonances of $+\Delta f$ and $-\Delta f$ are added to the frequency of a sweep pulse. As can be seen, an off-resonance shifts the pulse phase along both frequency and time (i.e., horizontally). Phase offsets (vertical shifts) also arise but are negligible (Supporting Information B), as they are readily removed from the data. However, the magnitude of the pulse spectrum is also shifted. Hence, to obtain uniform and similar excitation over the entire FOV, the frequency shift applied to each pulse should remain small compared with the imaging bandwidth $BW = \gamma\, G\, FOV$. In this work, rules for selecting the off-resonance are developed based on the condition number of the encoding matrix.

## 2.4 | Data acquisition

Imaging experiments were carried out on a 3T Achieva MRI scanner (Philips Healthcare, the Netherlands). Radiofrequency signal was created with a BLA-1000 amplifier (Bruker Biospin, France) with maximum output power of 1000 W, using either hard or hyperbolic secant sweep pulses for excitation.[20] Complementary short-$T_2$ optimized hardware included transmit-receive switches capable of switching in approximately 3 μs at 3 T,[27] a

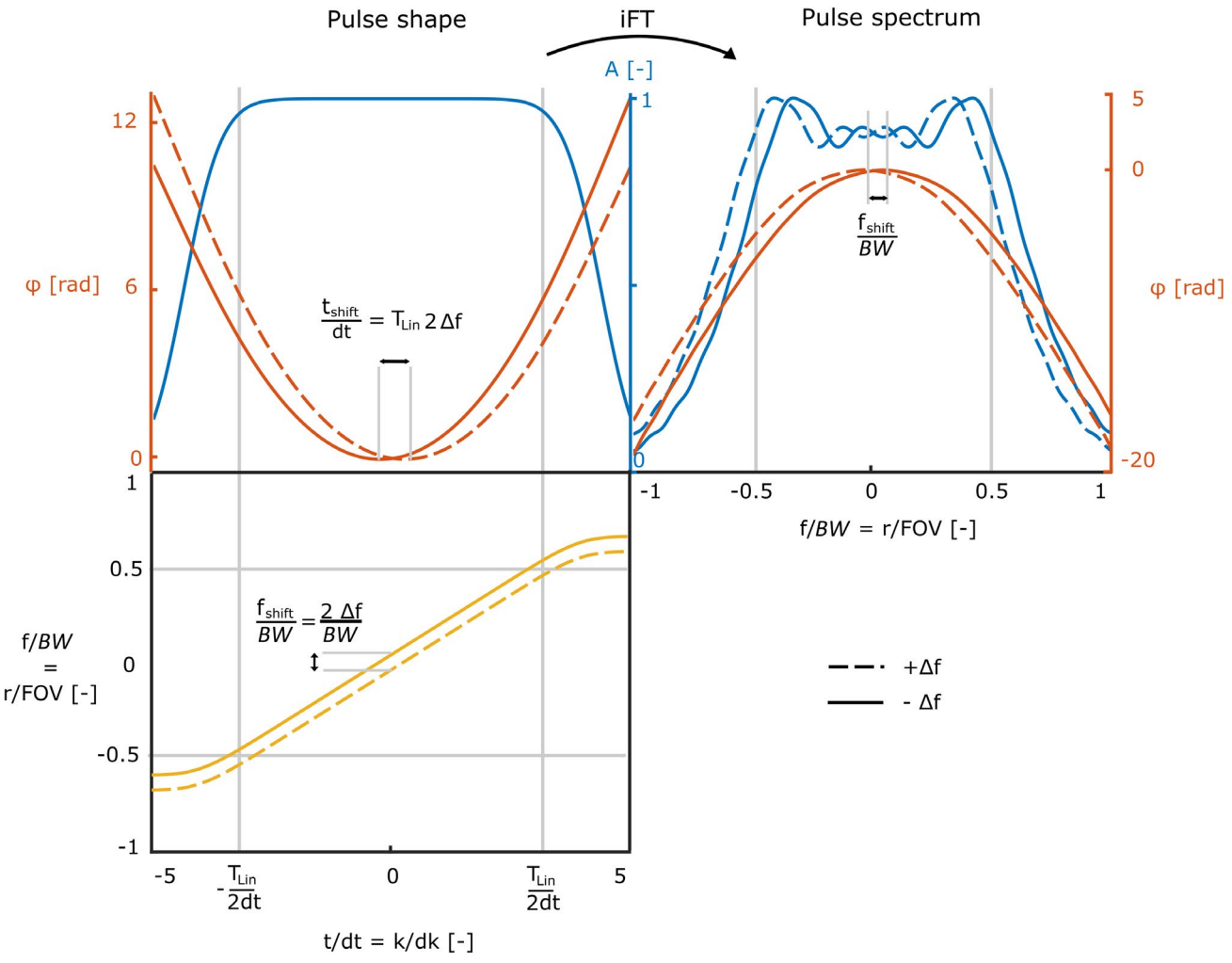


**FIGURE 4** Shapes and spectra of RF sweep pulses with off-resonance. Left: Two pulses of same duration (10 $dt$) but different off-resonances of $\pm\Delta f$ in their center frequency. Pulse amplitude $A$, phase $\phi$, and normalized frequency $f/BW$ are plotted as functions of time $t/dt$ expressed in Nyquist dwells $dt$. As opposed to the amplitude, which is unaffected by the off-resonance, both frequency and phase of the two pulses are shifted relative to each other. They are separated by $t_{shift}/dt = T_{Lin} 2\Delta f$ (Supporting Information B), with the time $T_{Lin}$ it takes to sweep the frequency linearly over the imaging bandwidth $BW$. Right: The pulse spectra, obtained by Fourier-transforming the pulse shapes, represent the excitation profiles in frequency and spatial domain. The applied off-resonances shift both magnitude and phase along the frequency axis, separating the two profiles by $f_{shift}/BW = 2\Delta f/BW$. Abbreviation: iFT, inverse Fourier transform

largely 1H-free birdcage resonator[28,29] and a custom-made spectrometer with up to 4-MHz acquisition bandwidth.[30] To take into account distortions introduced by the RF chain, pulses were measured with a pickup loop placed at a distance of approximately 1 m to the birdcage, using the same spectrometer and sampling as for MR data. A total of 10 000 averages were obtained during a total measurement time of 5 seconds. Only one of the two pulses per experiment was measured, and the second one was derived by applying the appropriate off-resonance.

Phantom images were taken on 1-L bottles filled with water and 3 mmol/L $CuSO_4$ and 0.15 mol/L $MnCl_2$ added, providing transverse relaxation times of several milliseconds and 77 μs, respectively. In the phantom experiments, the power of pulses of different length was adjusted such as to obtain equal flip angles according to the model of Kunz et al.[31] In vivo experiments were performed on a healthy volunteer according to applicable ethics approval and with written informed consent. Here, the flip angle for conventional ZTE was given by the hard pulse duration adjusted to *BW* and the available RF power. For PE-ZTE, the same power was used and the sweep pulse duration was maximized within constraints given by power deposition. For direct comparison of ZTE and PE-ZTE images, their total scan time was matched by adapting the number of averages. All imaging parameters are listed in Table 1. Additional noise data were acquired for SNR calculations.

## 2.5 | Image reconstruction

The reconstruction pipeline of PE-ZTE is equivalent to ZTE and sweep-ZTE (Figure 2). The only difference lies in the information provided in the encoding matrix $\boldsymbol{E}$, which includes two measured pulses in the case of PE-ZTE (Equation 6). Image SNR was calculated in two ways (Supporting Information C): (1) Local SNR was calculated by dividing the average intensity in a small 2D homogeneous region of interest (ROI) by the SD of the signal in the same ROI; and (2) global SNR was calculated by dividing the average intensity in a large 3D ROI by the SD of a reconstructed noise image in the same ROI.

# 3 | RESULTS

To investigate the sensitivity of PE-ZTE reconstruction to model violations such as noise or aliasing in dependence on the selected pulse off-resonance $\Delta f$, the condition number of the encoding matrix $\boldsymbol{E}$ was used as a significant and easily computable indicator. Figure 5A shows that the condition number plotted as a function of the off-resonance varies with pulse duration. However, a

**TABLE 1** Parameters of ZTE imaging experiments

| | Sequence parameters | | | | | | | | | RF pulse | | | | |
|---|---|---|---|---|---|---|---|---|---|---|---|---|---|---|
| Sample | Type | M | FOV [mm] | BW [kHz] | TR [ms] | $\Delta k_p$[dk] | $\Delta k_{T/R}$[dk] | Scan time [m:s] | NSA | Type | Dur. [μs] | Off-res. [kHz] | Power [W] | α [deg] |
| Long-$T_2$ bottle | ZTE | 150 | 260 | 320 | 1.5 | 0.48 | 0.90 | 02:34 | 2 | Hard | 3 | 0 | 1000 | 1 |
| | ZTE | 150 | 260 | 320 | 1.5 | 2.08 | 0.90 | 02:34 | 2 | Sweep | 13 | 0 | 285 | 1 |
| | PE | 150 | 260 | 320 | 1.5 | 2.08 | 0.90 | 01:17 (×2) | 1 (×2) | Sweep | 13 | ±25 | 285 | 1 |
| | ZTE | 150 | 260 | 320 | 1.5 | 4.96 | 0.90 | 02:34 | 2 | Sweep | 31 | 0 | 112 | 1 |
| | PE | 150 | 260 | 320 | 1.5 | 4.96 | 0.90 | 01:17 (×2) | 1 (×2) | Sweep | 31 | ±10 | 112 | 1 |
| Short-$T_2$ bottle | ZTE | 128 | 300 | 320 | 1.5 | 0.48 | 0.82 | 02:34 | 2 | Hard | 3 | 0 | 1000 | 1 |
| | PE | 128 | 300 | 320 | 1.5 | 4.96 | 0.82 | 01:17 (×2) | 1 (×2) | Sweep | 31 | ±10 | 112 | 1 |
| Head | ZTE | 250 | 260 | 300 | 2 | 0.45 | 0.85 | 19:28 | 6 | Hard | 3 | 0 | 1000 | 1 |
| | PE | 250 | 260 | 300 | 2 | 5.25 | 0.85 | 09:44 (×2) | 3 (×2) | Sweep | 35 | ±10 | 1000 | 3.5 |

Abbreviations: $BW = \gamma GFOV$, imaging bandwidth; M, reconstructed matrix size; NSA, number of signal averages; α, approximate flip angle.

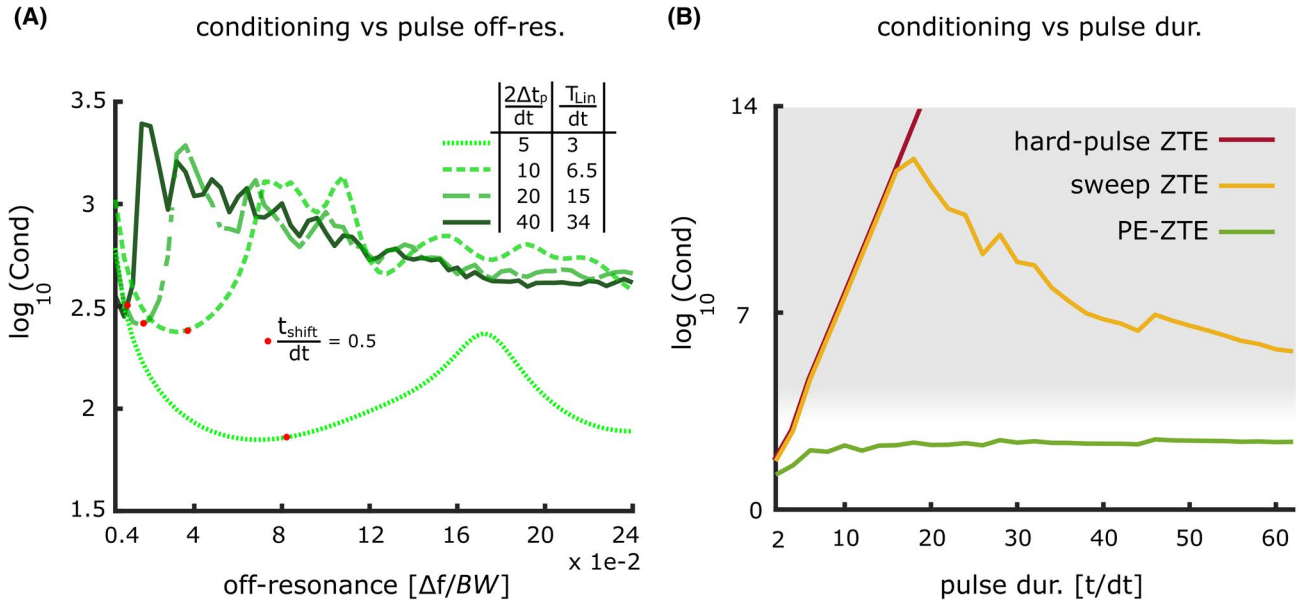


**FIGURE 5** Conditioning of ZTE reconstruction. For both plots, calculations were made with $\Delta t_{T/R}$= 1 *dt* and a matrix size of 128 pixels. (A) Pulse-encoded ZTE: The condition number of the encoding matrix $\boldsymbol{E}$ is plotted with logarithmic scale as a function of the normalized off-resonance $\Delta f/BW$, for different pulse lengths $2\Delta t_p/dt$ with corresponding linearity ranges $T_{Lin}/dt$. It is assumed that excitation is performed with two pulses of off-resonances $\pm\Delta f$, as shown in Figure 4. For each pulse duration, the conditioning has a first minimum near a location where the condition $t_{shift}/dt$ =0.5 is met. (B) Comparison of conditioning of hard-pulse ZTE, sweep ZTE, and PE-ZTE (assuming optimum off-resonance). The zone where images are dominated by noise amplification and aliasing is indicated in gray. In hard-pulse and sweep ZTE, the initial exponential increase of the condition number limits the usable pulse duration to 2–3 *dt*. In PE-ZTE, conditioning is only slightly dependent on pulse duration and remains below the gray zone, allowing the use of long pulses. Note that long hard pulses as considered in hard-pulse ZTE may not make sense on the excitation side, yet they still serve to reflect the behavior of the conditioning at large dead-time gaps

first minimum always occurs near $t_{shift} = 0.5\,dt$, i.e., when the time shift $t_{shift}$ of the pulse phase as associated with $\Delta f$ (Figure 4) equals half a Nyquist dwell. For the present case of two pulses with duration $T_{Lin}$ of the linear frequency sweep and with off-resonances $\pm\Delta f$, it holds that $t_{shift} = T_{Lin}2\Delta f\,dt$ (Supporting Information B). Hence, the near-optimal off-resonance is

$$\Delta f_{opt} = \frac{0.25}{T_{Lin}}. \tag{7}$$

Figure 5A also shows that the width of the valley enclosing the first minimum increases for decreasing pulse duration. Hence, for short pulses, the conditioning will be adequate over a broad range, and the smaller off-resonances should be preferred to favor uniform excitation.

In Figure 5B, the condition number is plotted as a function of the pulse duration for hard-pulse ZTE, sweep ZTE, and PE-ZTE. For the former two, the condition number increases exponentially and the pulse duration is limited to 2–3 *dt*. Around 15–20 *dt*, conditioning for sweep ZTE starts to improve again because neglecting excessively modulated coherences becomes effective (Supporting Information A), but it remains prohibitive. In PE-ZTE, conditioning is almost independent of the pulse duration, proving that the information lost during excitation can indeed be retrieved.

To gain a deeper insight into the mechanisms of ZTE reconstruction, Equation 1 was used to observe the coefficients of the linear combination applied in getting reconstructed k-space from acquired k-space, as illustrated in Figure 6A for a gap of 6 Nyquist dwells. Figure 6B-D shows the coefficients used by the reconstruction to compute the positive missing k-space points from the acquired data using different ZTE methods. Similar behavior is observed for excitation with a single hard or sweep pulse, confirming that sweep ZTE also uses predominantly finite support assumption to retrieve missing data. In these techniques, coefficients are extremely large, making them highly sensitive to model violations.

In contrast, in PE-ZTE (Figure 6D), the nonzero k-space points ($k/dk$ = 1–5) are reconstructed primarily from data located in a range of 5 *dt* following the dead time $\Delta t$ as expected from the signal model (Figure 3B). However, the k-space center ($k/dk = 0$) is reconstructed similarly as in sweep ZTE, i.e., showing relatively large side lobes (but still small in absolute numbers) over a wide data range of

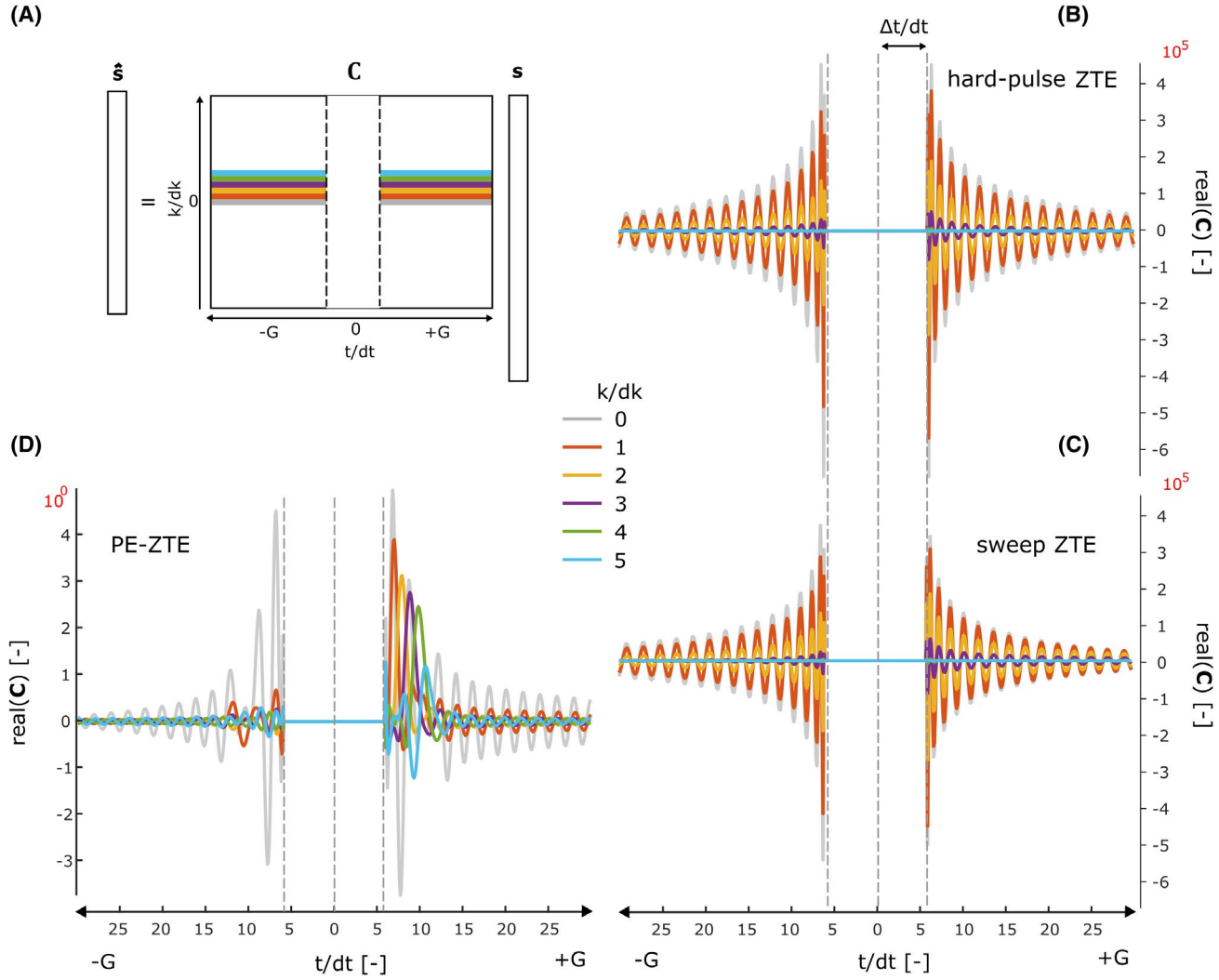


**FIGURE 6** Coefficients of linear combination used for k-space reconstruction. (A) Matrix $\boldsymbol{C}$ of Equation 1, transferring acquired data $\boldsymbol{s}$ to reconstructed data $\hat{\boldsymbol{s}}$ with highlighted lines at positive k-space locations with $0 \leq k/dk \leq 5$. B-D, Coefficients of $\boldsymbol{C}$ on the highlighted lines for ZTE with hard pulse (B), sweep ZTE (C), and PE-ZTE (D) with large differences in amplitude as indicated by the exponential factors shown in red. Acquisition parameters are as follows: $\Delta t = \Delta t_p + \Delta t_{T/R} = 5\,dt + 1\,dt = 6\,dt$, matrix size 128, and $\Delta f/BW = 0.04$

both gradient polarities. This suggests that the data are retrieved with finite support assumption, as it cannot be accessed through the pulse.

Long-$T_2$ phantom images obtained with PE-ZTE are shown in Figure 7 and compared to ZTE with hard and sweep pulses. With the latter two, clean images are obtained at the smallest gap, but amplified model violations due to aliasing of out-of-band signal emerge in the form of low-frequency background when $\Delta t$ approaches 3 $dt$, and dominate the image at $\Delta t = 6\,dt$. In contrast, PE-ZTE provides good image quality at all pulse lengths and gap sizes.

The short-$T_2$ imaging capability of PE-ZTE is illustrated in Figure 8 in comparison with hard-pulse ZTE. For both cases, the short-lived signal induces the same image blurring, as predicted by theory (Supporting Information A). Both techniques are comparable in terms of signal intensity, SNR and sharpness, demonstrating that PE-ZTE correctly recovers the signal lost during RF excitation, even with a decay constant on the order of the pulse duration.

The potential advantage of using longer pulses is illustrated in Figure 9, where PE-ZTE is used for head imaging and compared to conventional ZTE with hard pulse. As usual, the latter exhibits signal in short-$T_2$ tissues (e.g., bone) and robustness against distortions and signal loss (e.g., in the nasal cavities). However, the low flip angle as limited by maximum RF power and pulse duration leads to primarily proton density contrast, thus offering only minor information about the different tissue characteristics. However, with the about 3.5 times larger flip angle achievable with a long sweep pulse in PE-ZTE, two effects are observed. Generally, higher signal is obtained, as the Ernst angle is better approached for all tissues. Furthermore, $T_1$ weighting is introduced, leading to increased contrast (e.g., in the brain and in the eyes), and

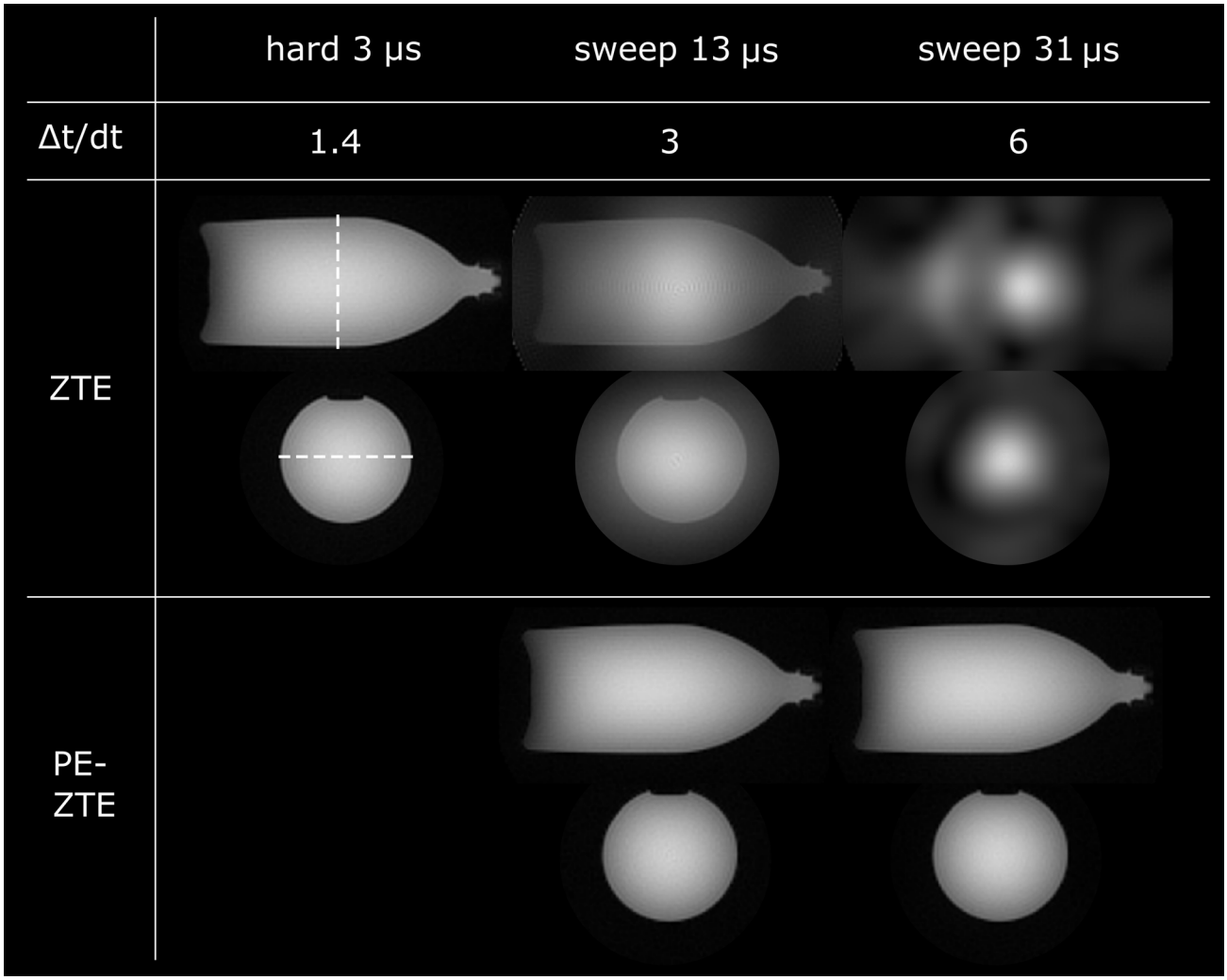


**FIGURE 7** Long-$T_2$ phantom imaging. A water bottle was scanned with hard-pulse ZTE, sweep ZTE, and PE-ZTE using increasing pulse durations, leading to different dead time gaps $\Delta t/dt$, including the same transmit-receive switch time $\Delta t_{T/R}/dt = 0.9$ for all images. Flip angles were kept constant by adapting the pulse power (Table 1). Orthogonal slices are shown at the locations indicated by the dashed lines. ZTE produces a clean image with the shortest (hard) pulse. However, as pulse length and dead time grow, the image is increasingly dominated by background artifacts. In PE-ZTE, image quality is maintained, even with long pulses

the signal of inflowing blood is also amplified. As noise performance is similar for both techniques, the signal gain nearly entirely translates into an equivalent SNR increase (Supporting Information C). Hence, for equal acquisition time, the overall SNR improves by about a factor of two in PE-ZTE as compared with hard-pulse ZTE.

The PE-ZTE image profiles in Figure 9 exhibit higher background signal than in hard-pulse ZTE. This is partly due to short-$T_2$ signal originating from the earmuffs, which is excited more efficiently with the sweep pulse. Additionally, a slight background artifact is present over the whole FOV with still unclear origin. Correlated, amplified noise can be excluded, as the effect is not observed in pure noise images (Supporting Information C). Other sources may be an altered aliasing behavior of short-$T_2$ compounds or coil ring down.

## 4 | DISCUSSION

In this work we introduce PE-ZTE, a novel method that exploits the intrinsic encoding properties of RF pulses to retrieve the data missed during spin excitation. Compared with conventional algebraic ZTE, it enables the use of longer pulses and thus can provide higher SNR and additional contrast.

Because in PE-ZTE the RF pulses are part of the encoding, to enable faithful image reconstruction, their shape as experienced by the sample should be known. This means in particular that distortions occurring in the RF chain must be assessed appropriately. This can be realized as in the present study by placing a pickup loop in the proximity of the imaging coil to measure the pulse shape as it arrives at the spins. As the actual measurement takes

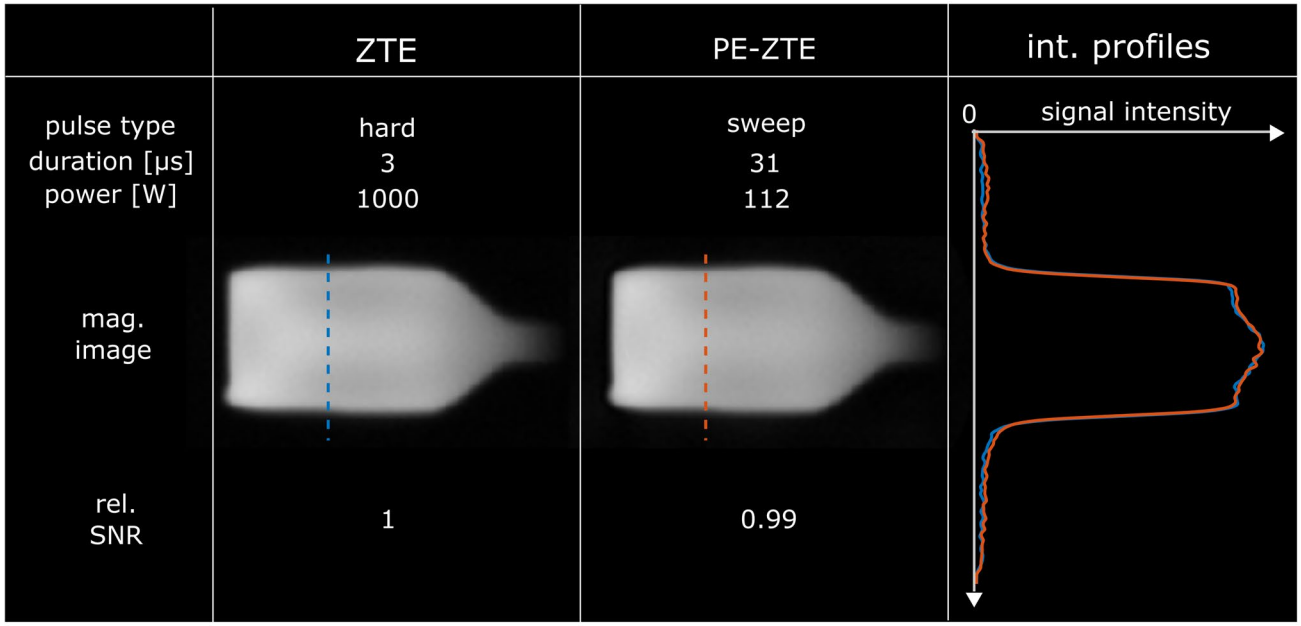


**FIGURE 8** Short-$T_2$ phantom imaging. A water bottle with $T_2^* \approx 77$ µs was scanned with hard-pulse ZTE and PE-ZTE. Flip angles were kept constant by adapting the pulse power (Table 1). Both techniques led to comparable image quality, sharpness, and SNR

only a few seconds, the overall experimental effort could be reduced by directly integrating a pickup loop into the imaging coil, as frequently done in commercial setups. As an alternative, NMR field probes in a dynamic field camera may be used to monitor RF pulses concurrently with the imaging experiment.[32] Moreover, the pulse shape may be deduced by other means. One approach would be to consider the RF chain a linear and time-invariant system (neglecting RF amplifier nonlinearity and changes in coil load) and to measure its transfer function. This could then be used to apply RF pre-emphasis to each pulse[33,34] or to calculate the actual pulse shape from its theoretical value. Another possibility would be to derive the pulse shape from the correlation between imaging data measured with equal gradient but different pulse encoding.

In the present implementation, PE-ZTE is performed with two complete ZTE data sets acquired with different pulses. In practice, a first complete data set is obtained with one pulse before executing the acquisition of the second data set with the other pulse (i.e., acquisitions are not interleaved). This option was chosen for ease of implementation but may be more sensitive to motion artifacts. Although it proved sufficiently robust for in vivo head imaging of a cooperative volunteer, clinical application of PE-ZTE would probably benefit from interleaved data acquisition. Generally, acquiring data twice can be seen as a major drawback. However, if averaging is needed anyway to obtain sufficient SNR, there is no penalty in this approach, which is the case for the head example of this work or many other ZTE applications such as myelin imaging,[10] lung imaging,[35] dental imaging,[4] and high-resolution imaging of other hard tissues.[36,37] On the contrary, in these cases PE-ZTE becomes advantageous, as larger flip angles allow for potentially increased SNR and enable $T_1$ contrast. On the other hand, if several averages are performed anyway, more than two different pulses could be used in PE-ZTE. However, so far no potential benefits in terms of conditioning or image quality have been perceived as compared with the two-pulses case.

If averaging is not required, the minimum scan time of PE-ZTE is indeed twice as large as for sweep ZTE. However, several solutions can be envisaged to overcome this limitation. First, the second data set could be acquired with angular undersampling by matching the number of spokes $N$ to the gap size ($N = 4\pi\ (\Delta t/dt)^2$) instead of the resolution ($N = 4\pi\ (M/2)^2$ with image matrix size $M$), similar to water-suppressed and fat-suppressed proton projection MRI, yet with maximum gradient strength. By aligning these spokes with the first acquisition, straightforward 1D reconstruction of the k-space center is enabled. In this case, the relative scan time required for the second acquisition amounts to $\left(2\Delta t/(Mdt)\right)^2$, which is typically on the order of a few percent only. Second, in radial acquisitions with angular Nyquist sampling, at least two-times oversampling occurs in the central k-space sphere of radius $\left(M/2\sqrt{2}\right)\ dk$. Hence, if spokes are excited in alternation with two different pulses, this k-space region will effectively be sampled twice, each time with independent pulse information. These kinds of data could then be merged in a full 3D PE-ZTE reconstruction, and no additional scan time would be required. Finally, another approach is to combine a single-sweep ZTE

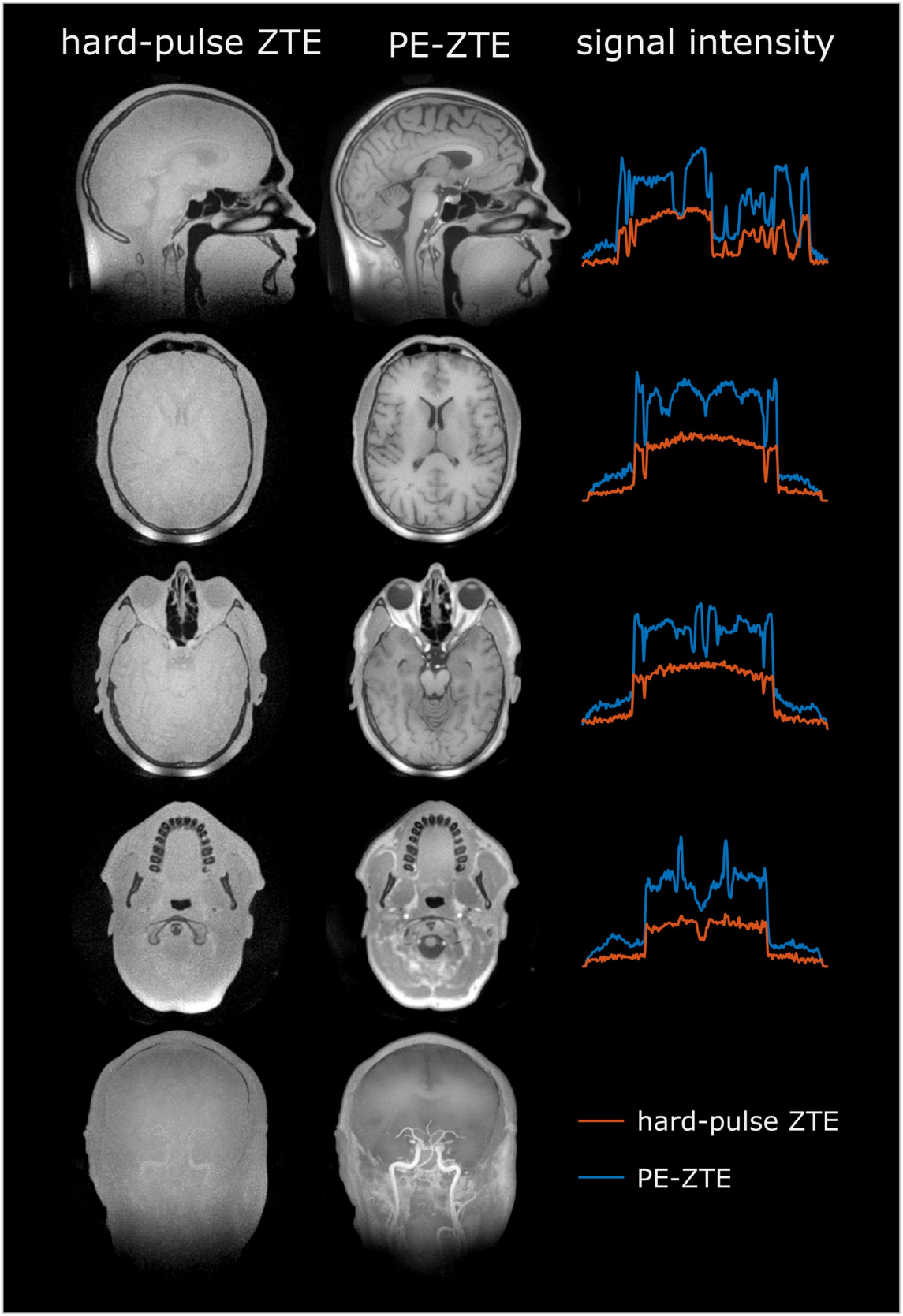


acquisition with SENSE, similar to what has been suggested for hard-pulse ZTE,[38,39] yet this time with longer sweep pulses. In this case, the effective excitation profiles result from a multiplication of the coil sensitivities with the pulse spectrum, making them different for each channel. Hence, according to the reasoning in Supporting

**FIGURE 9** In vivo head imaging. Conventional hard-pulse ZTE and PE-ZTE were compared with imaging parameters kept constant except for pulse type and duration (Table 1). Hard-pulse ZTE used a hard pulse of 3 μs and PE-ZTE a sweep pulse of 35 μs. The displayed resolution is 1.04 × 1.04 × 2.08 mm for a total scan time of 20 minutes. Both data sets were bias-corrected to remove $B_1$-related intensity variations. In hard-pulse ZTE, the small flip angle leads to primarily proton density contrast and limits the signal level. In PE-ZTE, the longer pulse increased the flip angle, leading to $T_1$ contrast in the brain between CSF, white matter, and gray matter. Also, in the eyes, the lenses appear with strong positive contrast. Furthermore, the larger flip angle increases in-flow contrast, leading to improved depiction of arterial vessels, as observed in both individual slices and the maximum intensity projection over a 7-cm-thick coronal slice (bottom row). Finally, the overall signal level is approximately doubled with PE-ZTE. The intensity profiles are measured horizontally and vertically centered in the FOV

Information A, the pulse information should be accessible when retrieving the missing data. However, the efficiency of this method compared with two-pulse PE-ZTE remains to be studied.

Considering only the signal model, the conditioning of PE-ZTE is relatively independent on pulse duration, even up to several tens of Nyquist dwells (Figure 5B). However, in practice, the pulse length may be limited by other factors. For example, the signal model assumes RF excitation to be linear, implying a Fourier relationship between pulse shape and spectrum, which is only considered sufficiently fulfilled for flip angles smaller than about 30°.[40] In addition, the pulse length is also bounded by limitations for the specific absorption rate, especially in the head as in the present study, or by restrictions of the average power applicable to RF hardware such as transmit-receive switches and coils. Finally, spurious signal from coil ring down in early data increases with pulse length and may translate into image artifacts (Supporting Information D). If such artifacts can be avoided, e.g., by using ringdown suppression techniques,[34] pulse durations would be limited to the maximum encoding time $t_{max} = M/2\,dt$ (Supporting Information A). However, with more involved reconstruction approaches, the use of even longer pulses may be feasible.

As described in Figure 3, the total dead time $\Delta t$ comprises half the pulse duration $\Delta t_p$ and the transmit-receive switching time $\Delta t_{T/R}$. With the approach introduced in this work, the data lost during $\Delta t_p$ can be recovered. However, data missed during $\Delta t_{T/R}$ must still be retrieved via finite support assumption as in conventional algebraic ZTE, hence limiting $\Delta t_{T/R}$ to 2–3 $dt$. Given recent advances in RF-switch design,[41] ringdown suppression[34] and data filtering strategies,[42] reducing $\Delta t_{T/R}$ and thus $\Delta t$ to the submicrosecond range is a realistic perspective. Thus, ZTE imaging with bandwidths in the Megahertz range without supplementary gap filling would be enabled.

In the PE-ZTE technique, the data correlation over the pulse duration is used for recovering data missed during the dead time. Beyond this, the correlation in the time domain may be further exploited to support other advanced signal–model-based ZTE reconstruction approaches, such as water–fat separation and $B_0$ mapping.[43,44]

With respect to ZTE-based sequences using direct gap filling such as PETRA, water-suppressed and fat-suppressed proton projection MRI, or ZTE with hybrid filling, PE-ZTE offers several advantages. To begin with, as no additional data acquisition of lower SNR efficiency is required, PE-ZTE will be beneficial, especially at large dead-time gaps. Furthermore, discontinuities in k-space weighting associated with $T_2^*$ decay and thus potential related image artifacts are avoided. Also, because the gradient magnitude is never lowered, quasi-continuous operation is enabled, thus reducing the sequence overhead. This allows the use of shorter TR, to make acquisitions more silent and to minimize eddy currents. In cases in which PE-ZTE is not usable due to excessive $\Delta t_{T/R}$, it could still be combined with direct gap-filling techniques, to decrease $\Delta t$ to $\Delta t_{T/R}$ and thereby reduce the time required to probe the inner k-space at lower gradient strength. In this case, image reconstruction would need to be performed fully in 3D.

The use of long sweep pulses is also a key element in sweep imaging with Fourier transformation.[25] However, in this technique, access to data during the pulse is enabled more directly by concurrent signal transmission and reception. Implementations of this concept use either repeated alternation between the two modes or true continuous operation,[45] which are, however, both technically highly demanding.

As soon as the recent advances in transmit-receive-switch design reach clinical scanners, PE-ZTE could become a useful tool for a broader community. Compared with other ZTE techniques, the longer minimum scan time will play against it for quick imaging that does not require averaging, e.g., when using low bandwidths and relatively long hard pulses. However, if high-resolution imaging of short-$T_2$ tissue is targeted, higher bandwidths will be required, rendering hard pulses inefficient. In such cases, also sweep-ZTE or sweep-PETRA with averaging could be used. However, PE-ZTE would probably be the better choice due to its greater robustness against artifacts related to model violations compared with sweep-ZTE, and its higher acquisition duty cycle and lower acoustic noise compared with PETRA.

## 5 | CONCLUSION

Algebraic reconstruction of ZTE data sets with large dead-time gaps was achieved by defining a new forward model that includes knowledge about multiple RF pulses. As opposed to conventional algebraic ZTE, image fidelity has only a minor dependence on pulse duration. Hence, longer sweep pulses may be used, potentially enabling significant improvements in SNR efficiency as well as $T_1$ contrast, even at high imaging bandwidth.

## CONFLICT OF INTEREST

Klaas P. Pruessmann holds a research agreement with and receives research support from Philips. He is a shareholder of Gyrotools LLC.

## ORCID

*Romain Froidevaux* https://orcid.org/0000-0001-7550-5554
*Klaas P. Pruessmann* https://orcid.org/0000-0003-0009-8362

## REFERENCES

1. Wehrli FW. Magnetic resonance of calcified tissues. *J Magn Reson*. 2013;229:35-48.
2. Cao H, Nazarian A, Ackerman JL, et al. Quantitative 31P NMR spectroscopy and 1H MRI measurements of bone mineral and matrix density differentiate metabolic bone diseases in rat models. *Bone*. 2010;46:1582-1590.
3. Gruwel MLH, Latta P, Tanasiewicz M, Volotovskyy V, Šramek M, Tomanek B. MR imaging of teeth using a silent single point imaging technique. *Appl Phys A Mater Sci Process*. 2007;88:763-767.
4. Weiger M, Pruessmann KP, Bracher AK, et al. High-resolution ZTE imaging of human teeth. *NMR Biomed*. 2012;25:1144-1151.
5. Kuethe DO, Caprihan A, Fukushima E, Waggoner RA. Imaging lungs using inert fluorinated gases. *Magn Reson Med*. 1998;39:85-88.
6. Johnson KM, Fain SB, Schiebler ML, Nagle S. Optimized 3D ultrashort echo time pulmonary MRI. *Magn Reson Med*. 2013;70:1241-1250.
7. Dournes G, Grodzki D, Macey J, et al. Quiet submillimeter MR imaging of the lung is feasible with a PETRA sequence at 1.5 T. *Radiology*. 2015;276:258-265.
8. Wilhelm MJ, Ong HH, Wehrli SL, et al. Direct magnetic resonance detection of myelin and prospects for quantitative imaging of myelin density. *Proc Natl Acad Sci USA*. 2012;109:9605-9610.
9. Du J, Ma G, Li S, et al. Ultrashort echo time (UTE) magnetic resonance imaging of the short T2 components in white matter of the brain using a clinical 3T scanner. *Neuroimage*. 2014;87:32-41.
10. Weiger M, Froidevaux R, Baadsvik EL, Brunner DO, Rösler MB, Pruessmann KP. Advances in MRI of the myelin bilayer. *Neuroimage*. 2020;217:116888.
11. Weiger M, Pruessmann KP. Short-T2 MRI: principles and recent advances. *Prog Nucl Magn Reson Spectrosc*. 2019;115:237-270.
12. Weiger M, Pruessmann KP. MRI with zero echo time. *Encycl Magn Reson*. 2012;1:311-322.
13. Weiger M, Brunner DO, Dietrich BE, Müller CF, Pruessmann KP. ZTE imaging in humans. *Magn Reson Med*. 2013;70:328-332.
14. Grodzki DM, Jakob PM, Heismann B. Ultrashort echo time imaging using pointwise encoding time reduction with radial acquisition (PETRA). *Magn Reson Med*. 2012;67:510-518.
15. Wu Y, Dai G, Ackerman JL, et al. Water- and fat-suppressed proton projection MRI (WASPI) of rat femur bone. *Magn Reson Med*. 2007;57:554-567.
16. Froidevaux R, Weiger M, Rösler MB, Brunner DO, Pruessmann KP. HYFI: hybrid filling of the dead-time gap for faster zero echo time imaging. *NMR Biomed*. 2021;34:1-14.
17. Froidevaux R, Weiger M, Brunner DO, Dietrich BE, Wilm BJ, Pruessmann KP. Filling the dead-time gap in zero echo time MRI: principles compared. *Magn Reson Med*. 2018;79:2036-2045.
18. Weiger M, Brunner DO, Tabbert M, Pavan M, Schmid T, Pruessmann KP. Exploring the bandwidth limits of ZTE imaging: spatial response, out-of-band signals, and noise propagation. *Magn Reson Med*. 2015;74:1236-1247.
19. Li C, Magland JF, Seifert AC, Wehrli FW. Correction of excitation profile in zero echo time (ZTE) imaging using quadratic phase-modulated RF pulse excitation and iterative reconstruction. *IEEE Trans Med Imaging*. 2014;33:961-969.
20. Schieban K, Weiger M, Hennel F, Boss A, Pruessmann KP. ZTE imaging with enhanced flip angle using modulated excitation. *Magn Reson Med*. 2014;74:684-693.
21. Weiger M, Hennel F, Pruessmann KP. Sweep MRI with algebraic reconstruction. *Magn Reson Med*. 2010;64:1685-1695.
22. Weiger M, Pruessmann KP, Hennel F. MRI with zero echo time: hard versus sweep pulse excitation. *Magn Reson Med*. 2011;66:379-389.
23. Kuethe DO, Caprihan A, Lowe IJ, Madio DP, Gach HM. Transforming NMR data despite missing points. *J Magn Reson*. 1999;139:18-25.
24. Pruessmann KP, Weiger M, Börnert P, Boesiger P. Advances in sensitivity encoding with arbitrary k-space trajectories. *Magn Reson Med*. 2001;46:638-651.
25. Idiyatullin D, Corum C, Park JY, Garwood M. Fast and quiet MRI using a swept radiofrequency. *J Magn Reson*. 2006;181:342-349.
26. Grodzki DM, Jakob PM, Heismann B. Correcting slice selectivity in hard pulse sequences. *J Magn Reson*. 2012;214:61-67.
27. Brunner DO, Furrer L, Weiger M, et al. Symmetrically biased T/R switches for NMR and MRI with microsecond dead time. *J Magn Reson*. 2016;263:147-155.
28. Weiger M, Brunner DO, Schmid T, et al. A virtually 1H-free birdcage coil for zero echo time MRI without background signal. *Magn Reson Med*. 2017;78:399-407.
29. Rösler MB, Weiger M, Brunner DO, Schmid T, Pruessmann KP. An RF birdcage coil designed for an insert gradient coil dedicated to short-T2 MRI. In: Proceedings of the 26th Annual Meeting of ISMRM, Honolulu, Hawaii, 2017. p 2668.
30. Dietrich BE, Brunner DO, Wilm BJ, et al. A field camera for MR sequence monitoring and system analysis. *Magn Reson Med*. 2016;75:1831-1840.
31. Kunz D. Use of frequency-modulated radiofrequency pulses in MR imaging experiments. *Magn Reson Med*. 1986;3:377-384.
32. Brunner DO, Dietrich BE, Çavuşoğlu M, et al. Concurrent recording of RF pulses and gradient fields—comprehensive field monitoring for MRI. *NMR Biomed*. 2016;29:1162-1172.

33. Chan F, Pauly J, Macovski A. Effects of RF amplifier distortion on selective excitation and their correction by prewarping. *Magn Reson Med*. 1992;23:224-238.
34. Brunner DO, Pruessmann KP. Coil ringdown suppression by broadband forward compensation. In: Proceedings of the 22nd Annual Meeting of ISMRM, Salt Lake City, Utah, 2014. p 951.
35. Gibiino F, Sacolick L, Menini A, Landini L, Wiesinger F. Free-breathing, zero-TE MR lung imaging. *Magn Reson Mater Phys Biol Med*. 2015;28:207-215.
36. Froidevaux R, Weiger M, Rösler MB, et al. High-resolution short-T2 MRI using a high-performance gradient. *Magn Reson Med*. 2020;84:1933-1946.
37. Baadsvik EL, Weiger M, Froidevaux R, et al. High-resolution MRI of mummified tissues using advanced short-T2 methodology and hardware. *Magn Reson Med*. 2021;85:1481-1492.
38. Roesler M, Weiger M, Brunner DO, Froidevaux R, Schmid T, Pruessmann K. An eight-channel array coil for zero echo time imaging. In: Proceedings of the 27th Annual Meeting of ISMRM, 2021. p 438.
39. Oberhammer T, Weiger M, Hennel F, Pruessmann KP. Prospects of parallel ZTE imaging. In: Proceedings of the 19th Annual Meeting of ISMRM, Montréal, Canada, 2011. p 2890.
40. Hoult DI. The solution of the Bloch equations in the presence of a varying B1 field-an approach to selective pulse analysis. *J Magn Reson*. 1979;35:69-86.
41. Schildknecht C, Weiger M, Froidevaux R, Pruessmann KP. Gallium nitride MOSFETs enable transmit-receive switching in less than 100 ns. In: Proceedings of the 29th Annual Meeting of ISMRM, 2021. p 1407.
42. Marjanovic J, Weiger M, Reber J, et al. Multi-rate acquisition for dead time reduction in magnetic resonance receivers: application to imaging with zero echo time. *IEEE Trans Med Imaging*. 2018;37:408-416.
43. Froidevaux R, Weiger M, Lu P, Pruessmann K. Signal-model-based water-fat separation in Zero Echo Time (ZTE) MRI. In: Proceedings of the 25th Annual Meeting of ISMRM, Honolulu, Hawaii, 2017. p 772.
44. Froidevaux R, Pruessmann KP. Advances in MRI with zero echo time. Doctoral Thesis. 10.3929/ethz-b-000453981. ETH Lib 2020.
45. Idiyatullin D, Suddarth S, Corum CA, Adriany G, Garwood M. Continuous SWIFT. *J Magn Reson*. 2012;220:26-31.


## SUPPORTING INFORMATION

Additional supporting information may be found in the online version of the article at the publisher's website.

**SUPPORTING INFORMATION A** Signal models and image reconstruction in algebraic zero-TE (ZTE) MRI. In this document, the ZTE signal model is shortly summarized and the mathematical basis of PE-ZTE are established

**SUPPORTING INFORMATION B** Calculation of phase shift in frequency-swept RF pulses induced by off-resonance in center frequency. This document contains the mathematical derivation of the phase shift induced by an off-resonance in the center frequency of a frequency-swept pulse

**SUPPORTING INFORMATION C** Signal-to-noise calculations. This document details the methods used to calculate the SNR in the head images

**SUPPORTING INFORMATION D** Experimental limitation of PE-ZTE. This document illustrates the current experimental limitation of the pulse duration in PE-ZTE imaging

**How to cite this article:** Froidevaux R, Weiger M, Pruessmann KP. Pulse encoding for ZTE imaging: RF excitation without dead-time penalty. *Magn Reson Med*. 2022;87:1360–1374. doi:10.1002/mrm.29056